

A Diffuse Interface Model for Electrowetting Droplets In a Hele-Shaw Cell

By H.-W. LU¹, K. GLASNER³, A. L. BERTOZZI², AND C.-J. KIM¹

¹Department of Mechanical and Aerospace Engineering, UCLA, Los Angeles, CA 90095, USA

²Department of Mathematics, UCLA, Los Angeles, CA 90095, USA

³ Department of Mathematics, University of Arizona, Tucson, AZ 85721, USA

(Received 2 July 2005)

Electrowetting has recently been proposed as a mechanism for moving small amount of fluids in confined spaces. We proposed a diffuse interface model for droplet motion, due to electrowetting, in Hele-Shaw geometry. In the limit of small interface thickness, asymptotic analysis shows the model is equivalent to Hele-Shaw flow with a voltage-modified Young-Laplace boundary condition on the free surface. We show that details of the contact angle significantly affect the time-scale of motion in the model. We measure receding and advancing contact angles in the experiments and derive its influences through a reduced order model. These measurements suggest a range of timescales in the Hele-Shaw model which include those observed in the experiment. The shape dynamics and topology changes in the model, agree well with the experiment, down to the length scale of the diffuse interface thickness.

1. Introduction

The dominance of capillarity as an actuation mechanism in the micro-scale has received serious attention recently. Darhuber & Troian (2005) recently reviewed various

microfluidic actuators by manipulation of surface tension. Due to the ease of electronic control and low power consumption, electrowetting has become a popular mechanism for microfluidic actuations. Lippman (1875) first studied electrocapillary in the context of a mercury-electrolyte interface. The electric double layer is treated as a parallel plate capacitor,

$$\gamma_{sl}(V) = \gamma_{sl}(0) - \frac{1}{2}CV^2, \quad (1.1)$$

where C is the capacitance of the electric double layer, and V is the voltage across the double layer. Kang (2002) calculated the electro-hydrodynamic forces of a conducting liquid wedge on a perfect dielectric, and recovered equation (1.1). The potential energy stored in the capacitor is expended toward lowering the surface energy. However, the amount of applicable voltage is limited by the low breakdown voltage of the interface. Inserting a layer of dielectric material between the two charged interfaces alleviates this difficulty without much voltage penalty and makes electrowetting a practical mechanism of micro-scale droplet manipulation (see Moon, Cho, Garrel & Kim 2004). Experimental studies have revealed saturation of the contact angle when the voltage is raised above a critical level. The cause of the saturation is still under considerable debate. Peykov, Quinn & Ralston (2000) modelled saturation when the liquid-solid surface energy reaches zero. Verheijen & Prins (1999) proposed charge trapping in the dielectric layer as a saturation mechanism. Seyrat & Hayes (2001) suggested the dielectric material defects as the cause of saturation. Vallet, Vallade & Berge (1999) observed ejection of fine droplets and luminescence due to air ionization. The loss of charge due to gas ionization is proposed as the cause of saturation. Despite the saturation of contact angle, engineers have successfully developed a wide range of electrocapillary devices. Pollack, Fair & Shenderov (2000) first demonstrated droplet actuation by electrowetting in fluid-filled Hele-Shaw cell. Lee, Moon, Fowler, Schoellhammer & Kim (2002*b*) developed droplet actuation in

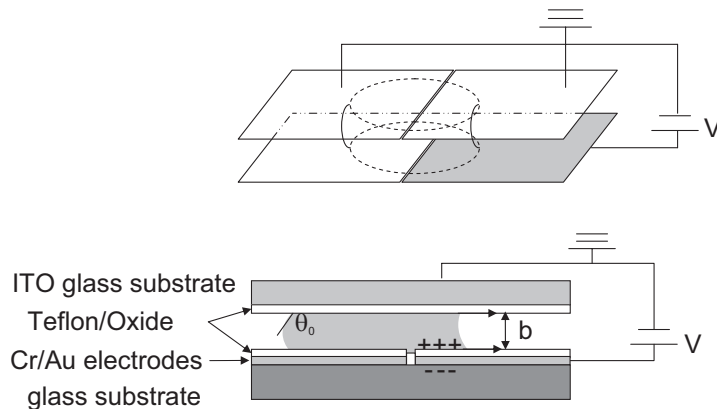


FIGURE 1. Illustration of electrowetting device.

a dry Hele-Shaw cell. Hayes & Feenstra (2003) utilized the same principle to produce a video speed display device.

The electrowetting device we consider is shown in figure 1. It consists of a fluid droplet constrained between two solid substrates separated by a distance, b . The bottom substrate is patterned with a silicon oxide layer and gold electrodes. Both substrates are coated with a thin layer of fluoropolymer to increase liquid-solid surface energy. For simplicity, we neglect the thin fluoropolymer coating on the top substrate. Cho, Moon & Kim (2003) and Pollack, Shenderov & Fair (2002) demonstrated capabilities to transport, cut, and merge droplets in similar devices. The aspect ratio of the droplet, $\alpha = b/R$, can be controlled by droplet volume and substrate separation. Here we consider experiments where $\alpha \leq 0.1$ with scaled Reynolds number $Re^* = Re * \alpha^2 \sim 0.01$.

For a constrained droplet of radius R much greater than the droplet height b , the geometry approximates a Hele-Shaw cell (see Hele-Shaw 1898) for which one can use lubrication theory to provide a simple model. Taylor & Saffman (1958) and Chouke, van Meurs & van der Poel (1959) studied viscous fingering in a Hele-Shaw cell as a model problem for immiscible fluid displacement in a porous medium. Experiments of a less

viscous fluid displacing a more viscous fluid initially showed the development of multiple fingers. Over the long time scale, one finger gradually grows to approximately half of the channel width at the expense of the other fingers. On the contrary, the theoretical model allows the development of fingers with a continuous spectrum of width. In addition, stability analysis shows the observed stable fingers are unstable to infinitesimal disturbances. This paradoxical result sparked 50 years of investigations into the fluid dynamics in a Hele-Shaw cell. Advances in this field are well reviewed in literature (see Saffman 1986; Homsy 1987; Bensimon, Kadanoff, Liang & Shraiman 1986; Howison 1992; Tanveer 2000). One problem that has been extensively studied is the fluid dynamics of a bubble inside a Hele-Shaw cell in the absence of electrowetting. Taylor & Saffman (1959) considered a bubble with zero surface tension and found two families of bubble shapes parameterized by the bubble velocity and area. Tanveer (1986, 1987) and Tanveer & Saffman (1987) solved the equations including small surface tension and found multiple branches of bubble shapes parameterized by relative droplet size, aspect ratio, and capillary number.

Despite the extensive theoretical investigation, experimental validation of the bubble shapes and velocities has been difficult due to the sensitivity to the conditions at the bubble interface. Maxworthy (1986) experimentally studied buoyancy driven bubbles and showed a dazzling array of bubble interactions at high inclination angle. He also observed slight discrepancies of velocity with the theory of Taylor & Saffman (1959) and attributed it to the additional viscous dissipation in the dynamic meniscus. For pressure driven fluid in a horizontal cell, Kopfsill & Homsy (1988) observed a variety of unusual bubble shapes. In addition, they found nearly circular bubbles travelling at a velocity nearly an order of magnitude slower the theoretical prediction. Tanveer & Saffman (1989) qualitatively attributed the disagreement to perturbation of boundary conditions due to contact angle

hysteresis. Park, Maruvada & Yoon (1994) suggests the velocity disagreement and the unusual shapes may be due to surface-active contaminants. In these studies, the pressure jump at the free surface was determined from balancing surface tension against the local hydrodynamic pressure that is implicit in the fluid dynamics problem. Electrowetting provides an unique way to directly vary the pressure on the free boundary. Knowledge of the electrowetting droplet may provide a direct means to investigate the correct boundary condition for the multiphase fluid dynamics in a Hele-Shaw cell.

Due to the intense interest in the Hele-Shaw problems, the last ten years has also seen a development of numerical methods for Hele-Shaw problem. The boundary integral method developed by Hou, Lowengrub & Shelly (1994) has been quite successful in simulating the long time evolution of free boundary fluid problems in a Hele-Shaw cell. However, simulating droplets that undergo topological changes remains a complicated, if not ad hoc, process for methods based on sharp interfaces. Diffuse interface models provide alternative descriptions by defining a phase field variable that assumes a distinct constant value in each bulk phase. The material interface is considered as a region of finite width in which the phase field variable varies rapidly but smoothly from one phase value to another. Such diffuse interface methods naturally handle topology changes. As we demonstrate in this paper, an energy construction provides a convenient framework in which to incorporate a spatially varying surface energy due to electrowetting. Formal asymptotics may be used to demonstrate the equivalence between the diffuse interface dynamics and the sharp interface dynamics in the Hele-Shaw cell.

In this paper we develop a diffuse interface framework for the study of Hele-Shaw cell droplets that undergo topological changes by electrowetting. Using level set methods Walker & Shapiro (2004) considered a similar problem with the addition of inertia. We consider a flow dominated by viscosity inside the droplet. The related work of Lee, Lowen-

material	thickness (\AA)	dielectric constant
substrate height	$(529 \pm 2) \times 10^4$	n/a
silicon dioxide	4984 ± 78.08	3.8
fluoropolymer	2458 ± 155.16	2.0

TABLE 1. Layer dimensions and dielectric constants of electrowetting device.

grub & Goodman (2002*a*) considered a diffuse interface in the absence of electrowetting in a Hele-Shaw cell under the influence of gravity. They used a diffuse interface model for the chemical composition, coupled to a classical fluid dynamic equation. Our model describes both the fluid dynamics and the interfacial dynamics through a nonlinear Cahn-Hilliard equation of one phase field variable. Our approach expands on the work done by Glasner (2003) and is closely related to that of Kohn & Otto (1997); Otto (1998).

§2 describes the experimental setup of droplet manipulation using electrowetting. §3 briefly reviews the sharp interface description of the fluid dynamics of electrowetting in Hele-Shaw cell. We also discuss briefly the role of the contact line in the context of this model. In §4, we describe the diffuse interface model of the problem. Equivalence with the sharp interface model will be made in §5 through matched asymptotic expansions. Comparisons will be made in §6 between the experimental data and the numerical results. Finally, we comment on the influence of various experimental conditions on the dynamic timescale in §7, followed by conclusions.

2. Experimental setup

2.1. Procedure

The fabrication of electrowetting devices is well documented in previous studies (see Cho *et al.* 2003; Wheeler *et al.* 2004). Unlike the previous work, we enlarge the device geome-

try by a factor of 10 and use a more viscous fluid such as glycerine to maintain the same Reynolds number as in the smaller devices. Such modification allows us to more carefully maintain the substrate separation and to directly measure the contact angle. Our devices have electrodes of size 1 cm and are fabricated in the UCLA Nanolab. The 60% glycerine-water mixture by volume is prepared with deionized water. The surface tension and viscosity of the mixture are measured to be 0.02030 Pa s and 66.97 dyne cm⁻¹ respectively. The relevant device dimensions are summarized in table 1. A droplet with aspect ratio of approximately 0.1 is dispensed on top of an electrode in the bottom substrate (see figure 1). The top substrate then covers the droplet, with two pieces of silicon wafers maintaining the substrate separation at 500 μm . The entire top substrate and the electrode below the droplet are grounded. Application of an electrical potential on an electrode next to the droplet will draw the droplet over to that electrode. The voltage level is cycled between 30 V DC and 70 V DC. Images of the droplet motions are collected in experiments conducted at 50 V DC. A camera is used to record the motion from above at 30 frames per second. Side profiles of the droplet are recorded by a high speed camera (Vision Research Inc., Wayne, NJ) at 2000 frames per second. The images are processed by Adobe [®] photoshop and Matlab [®] for edge detection.

2.2. Observations

Three different droplet behaviors were observed. At low voltage, a slight contact angle change is observed but the contact line remains pinned as shown in figure (2a) until a threshold voltage is reached. The threshold voltage to move a 60% glycerine-water droplet is approximately 38 V DC. The free surface remains smooth for voltage up to 65 V DC as shown in figure (2b). At higher voltage, we observed irregularities of the liquid-vapor interface such as the one shown in figure (2c) with stick-slip interface motion. When the voltage is ramped down, the motion of the droplet becomes much slower, suggesting

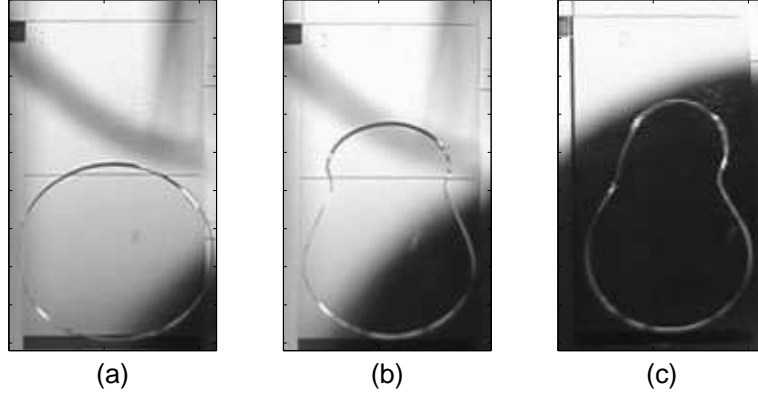


FIGURE 2. Behaviors of droplets under different voltage. (a) The droplet remains motionless at low voltage level (30.23 V DC). (b) The droplet advances with smoothly at 50.42 V DC. (c) Irregularities of the advancing interface is observed at 80.0 V DC.

some charge trapping in the dielectric materials. Experiments repeated at 50 V DC shows relatively constant droplet speed. Time indexed images of the droplet translation and splitting are compared against the simulation results in figure 8 and figure 9 in §6. For 60% glycerine liquid, the droplet moves across one electrode in approximately 3 seconds. We estimated a capillary number of $Ca \approx 10^{-3}$ using mean velocity.

To fully understand the problem we must also measure the effect of electrowetting on contact angles in the cell. The evolution of the advancing meniscus is shown in figure 3. The thick dielectric layer on the bottom substrate causes significant contact angle change on the bottom substrate due to electrowetting. The top substrate, which does not have a thick dielectric layer, is unaffected by the applied voltage. Pinning of the contact line is clearly observed along the top substrate. The hysteretic effect causes the initially concave meniscus to quickly become convex. The contact angles appear to converge toward a steady state value as shown in figure 4. However, the magnification requirement prevents us from monitoring the evolution of the contact angles over a longer timescale. The direct observation by the camera can only reveal the contact angles at two

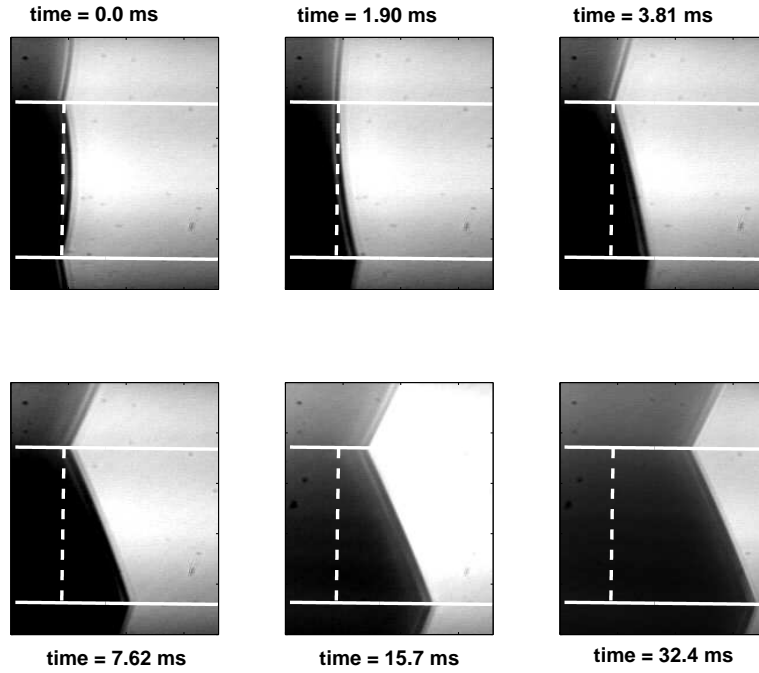


FIGURE 3. Advancing meniscus of a drop of 60% glycerine. The solid lines depict the top and bottom substrates. $V = 50.28$ volts.

points of the curvilinear interface. Along the interface, the capillary number varies with the normal velocity of the interface. Therefore, we expect the dynamic contact angle to vary along the interface. Better experimental techniques are required to characterize the evolution of the dynamic contact angle on the entire interface.

3. Sharp interface description

Here we review the classical model of Hele-Shaw fluid dynamics (see Taylor & Saffman 1959, 1958) and extend the model to include electrowetting. Consider a droplet in a Hele-Shaw cell shown in figure 5 occupying a space $[\Omega \times b]$, where b is the distance between the substrates. The reduced Reynolds number, $Re^* = Re * \alpha^2$ is of the order $O(10^{-2})$. This allows us to employ a lubrication approximation to reduce the momentum equation

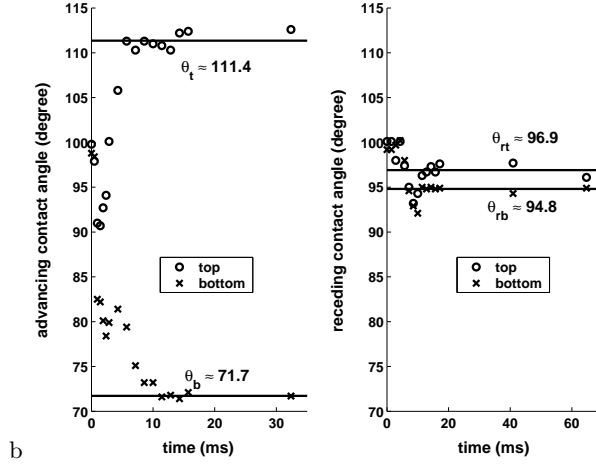


FIGURE 4. Evolution of the advancing and receding contact angles.

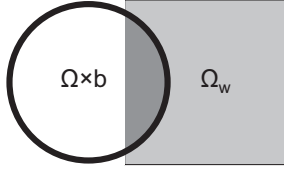


FIGURE 5. Top down view of a droplet inside of a electrowetting device.

to Darcy's law coupled with a continuity equation,

$$\mathbf{U} = -\frac{b^2}{12\mu} \nabla P, \quad (3.1)$$

$$\nabla \cdot \mathbf{U} = 0, \quad (3.2)$$

where \mathbf{U} is the depth-averaged velocity, P is the pressure, and μ is the viscosity. Equations (3.1) and (3.2) imply the pressure is harmonic, $\Delta P = 0$.

The interfacial velocity is the fluid velocity normal to the interface, $\mathbf{U}_n \sim \nabla P|_{\partial\Omega} \cdot \hat{\mathbf{n}}$. The boundary condition for normal stress depends on the interactions between the different dominant forces in the meniscus region. Assuming ambient pressure is zero,

$$P|_{\partial\Omega} = \gamma_{lv} (A\kappa_0 + B\kappa_1). \quad (3.3)$$

κ_0 , defined as $1/r$, is the horizontal curvature and κ_1 is defined as $2/b$. Different dynamics

and wetting conditions at the meniscus determine the actual curvatures of the droplet through A and B . For a static droplet with 180 degrees contact angle, $A = 1$ and $B = 1$. For a bubble in motion, (Chouke, van Meurs & van der Poel 1959) and Taylor & Saffman (1959) made the assumptions that

$$A = 1, \quad (3.4)$$

$$B = -\cos \theta_0, \quad (3.5)$$

where θ_0 is the apparent contact angle. The appropriateness of this boundary condition has been investigated in several studies. In a study of long bubbles in capillary tubes filled with wetting fluids ($\theta_0 = \pi/2$), Bretherton (1961) showed that $B = 1 + \beta Ca^{2/3}$, in agreement with (3.5) to the leading order. In addition, he derived the value of β to be 3.8 and -1.13 for advancing and receding menisci respectively. For Hele-Shaw bubbles surrounded by wetting fluids, Park & Homsy (1984) and Reinelt (1987) confirm the result of Bretherton (1961) and showed that $A = \pi/4 + O(Ca^{2/3})$, which disagrees with (3.4). In absence of electrowetting, the cross substrate curvature, $B\kappa_1$, does not effect the dynamics significantly, since it remains constant to the leading order. Therefore, the value of A has a significant effect on the dynamic timescale.

When a voltage is applied across an electrode, $V(x) = V\chi(x)$, where $\chi(x)$ is a characteristic function of the electrode, Ω_w , it locally decreases the solid-liquid surface energy inside the region $\Omega_w \cap \Omega$

$$\gamma_w(V) = \gamma_{lv} \left(-\cos \theta_0 - \frac{CV^2}{2\gamma_{lv}} \right), \quad (3.6)$$

where $\gamma_w(V)$ is the difference between the liquid-solid and the solid-vapor surface energy. In deriving (3.6), we assume the electrowetting does not affect the solid-vapor surface energy. Most of the voltage drop occurs across the thick dielectric layer on the bottom substrate, resulting a significant change in the surface energy. On the top substrate, the

surface energy remains unchanged. The total solid-liquid interfacial energy in the device is

$$\gamma_{dev} = \gamma_{lv} \left(-2 \cos \theta_0 - \frac{CV^2}{2\gamma_{lv}} \right). \quad (3.7)$$

Using Young's equation, we relate the change in contact angle to the electrowetting voltage,

$$\cos \theta_v = \cos \theta_0 + \frac{CV^2}{2\gamma_{lv}}. \quad (3.8)$$

We assume the voltage under consideration is below saturation so that equation (3.8) is valid. The dominance of surface tension allows us to assume a circular profile for the liquid-vapor interface. Substituting (3.8) into (3.7) gives

$$\gamma_{dev} = \gamma_{lv} (-\cos \theta_0 - \cos \theta_v) = \gamma_{lv} b \kappa_w, \quad (3.9)$$

where $\kappa_w = (-\cos \theta_0 - \cos \theta_v)/b$ is the curvature of the cross substrate interface in the presence of electrowetting. The constant $\cos \theta_0$ does not effect the dynamics, so we will consider it to be zero. Substituting (3.8) for $\cos \theta_v$ in κ_w shows $B = -CV^2/4\gamma_{lv}$.

For a droplet of volume v placed inside of a Hele-Shaw cell with plate spacing of b , the radius is $R = (v/\pi b)^{1/2}$. We non-dimensionalize the Hele-Shaw equations by the following scales:

$$r \sim R\tilde{r}, \quad t \sim \frac{12\mu R}{\gamma_{lv}\alpha^2}\tilde{t}, \quad P \sim \frac{\gamma_{lv}}{R}\tilde{P}, \quad (x, y, z) \sim (R, R, b). \quad (3.10)$$

Removing the $\tilde{\cdot}$ gives the following equations in dimensionless variables:

$$\Delta P = 0, \quad (3.11)$$

$$\mathbf{U} = -\nabla P, \quad (3.12)$$

$$P|_{\partial\Omega} = A\kappa_0 + B\kappa_1, \quad (3.13)$$

$$\mathbf{U}_n = \nabla P|_{\partial\Omega} \cdot \hat{\mathbf{n}}. \quad (3.14)$$

In dimensionless terms, $\kappa_1 = 2/\alpha$ reflects the ratio between liquid-vapor and solid-liquid

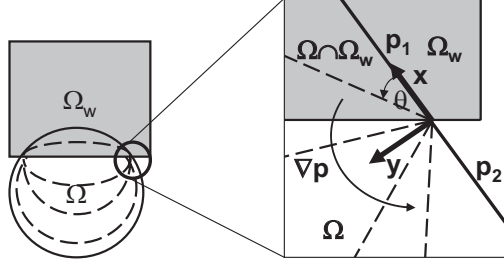


FIGURE 6. Illustration of electrowetting acting on a circular droplet and the details near the boundary of electrode. Dashed lines depict the pressure contours.

interfacial areas, and $B = -CV^2/4\gamma_{lv}$ reflects the ratio of the associated surface energies. $B\kappa_1$, dominates the pressure boundary condition of an electrowetting droplet due to the small aspect ratio, α . Without the applied voltage, $V = B = 0$, the constant $A = \pi/4$ may be incorporated into the scaling. Therefore, the classical Hele-Shaw model has no dimensionless parameters, meaning the relaxation of all Hele-Shaw droplets starting from similar initial conditions can be collapsed to the same problem in dimensionless form.

The locally applied voltage induces convective motion toward Ω_w and extends the liquid-vapor interface. The surface tension acts concurrently to minimize the interface area. This interaction introduces one dimensionless parameter to the classical Hele-Shaw flow. We define the electrowetting number

$$\omega = -B\kappa_1 = \frac{CV^2}{2\alpha\gamma_{lv}}. \quad (3.15)$$

as the relative measure between the driving potential of the electric double layer and the total energy of the liquid-vapor interface.

Let us consider the effect of a force that causes a discontinuous change of the cross substrate curvature and the pressure as shown in figure 6. The pressure on the droplet boundary is equal to the change in the curvature, $(P_2 - P_1) = -[B\kappa_1]$ and the pressure field must satisfy the Laplace's equation. Therefore, the pressure field depends only on

the polar angle from the contact line. In the neighborhood of such discontinuity, the pressure and the velocity in the locally orthogonal coordinates, \mathbf{x} , and \mathbf{y} , are

$$P = -\frac{[B\kappa_1]}{\pi} \arctan\left(\frac{y}{x}\right) + P_1, \quad (3.16)$$

$$U = -\nabla P = \frac{[B\kappa_1]}{\pi} \frac{(-y\hat{\mathbf{i}} + x\hat{\mathbf{j}})}{x^2 + y^2}. \quad (3.17)$$

Equation (3.17) shows that $U \sim [B\kappa_1]$. Therefore, $[B\kappa_1]$ dictates the convective timescale of the electrowetting. Away from $\partial\Omega_w$ where $B\kappa_1$ is relatively constant, the droplet relaxes to minimize the liquid-vapor interface and $A\kappa_0$ dictates the relaxation timescale. The dynamics of the droplet motion is determined by the relative magnitude between the two timescales. Therefore, we will maintain the variables A and B throughout the discussion.

In applying the electrowetting model (3.15) for $[B\kappa_1]$, we assume the contact angles are determined from a quasi-static balance between the surface energies and the electrical potential. The presence of moving contact lines introduces deviations from the equilibrium values. In §7, we will introduce the complication of contact line dynamics through the local dependence of A and B on the dynamic contact angles.

4. Diffuse interface model

Diffuse interface (phase field) models have the advantage of automatically capturing topological changes such as droplet splitting and merger. Here we extend Glasner's (2003) diffuse interface model to include electrowetting. The model begins with a description of the surface energies in terms of a "phase" function ρ that describes the depth-average of fluid density in a cell. Therefore $\rho = 1$ corresponds to fluid and $\rho = 0$ to vapor. Across the material interface, ρ varies smoothly over a length scale ϵ .

The total energy is given by the functional

$$E(\rho) = \int_{\Omega} \frac{A}{\gamma} \left(\frac{\epsilon}{2} |\nabla \rho|^2 + \frac{g(\rho)}{\epsilon} \right) - \rho \omega dx. \quad (4.1)$$

The first two terms of the energy functional approximate the total liquid-vapor surface energy $\int_{\partial\Omega} \gamma dS$ where $\partial\Omega$ is the curve describing the limiting sharp interface. An interface between liquid and vapor is established through a competition between the interfacial energy associated with $|\nabla \rho|^2$ and the bulk free energy $g(\rho)$ that has two equal minima at ρ_l and ρ_v . To avoid the degeneracy in the resulting dynamic model (see equations 4.7-4.8) and to maintain consistency with the desired sharp-interface limit, we choose $\rho_l = 1$ and $\rho_v = \epsilon$. The final term $\rho\omega$ accounts for the wall energy (the difference between the solid-liquid and solid-vapor surface energies) on the solid plates. The first two terms act as line energies around the boundary of the droplet while the third term contributes the area energy of the solid-liquid interfaces.

In equation (4.1), γ is a normalization parameter which we discuss below. A 1-D equilibrium density profile can be obtained by solving the Euler-Lagrange equation of the leading order energy functional in terms of a scaled spatial coordinate, $z = x/\epsilon$,

$$(\rho_0)_{zz} - g'(\rho_0) = 0, \quad (4.2)$$

which has some solution $\phi(z)$ independent of ϵ that approaches the two phases ρ_l, ρ_v as $z \rightarrow \pm\infty$. Integrating equation (4.2) once gives

$$\frac{\epsilon}{2} \phi_x^2 = \frac{g(\phi)}{\epsilon}. \quad (4.3)$$

Equation (4.3) implies equality between the first and second terms of the energy functional so the total liquid-vapor interfacial energy can be written as

$$\gamma = \int_{-\infty}^{\infty} (\phi)_z^2 dz = 2 \int_{-\infty}^{\infty} g(\phi) dz. \quad (4.4)$$

Equation (4.4) indicates the choice of $g(\phi)$ used to model the bulk free energy influ-

ences the amount of interfacial energy in the model. Hence this constant appears as a normalization parameter in the first two terms of the energy functional (4.1).

Since there is no inertia in the physical system, the dynamics take the form of a generalized gradient flow of the total energy, which can be equivalently characterized as a balance between energy dissipation and the rate of free energy change,

$$D \approx \int_{R^2} \rho |\mathbf{U}|^2 dx dy. \quad (4.5)$$

Since ρ is conserved, $\rho_t = -\nabla \cdot (\rho \mathbf{U})$. Using this fact and equating the rate of energy dissipation to the rate of energy change gives

$$\int_{R^2} \rho |\mathbf{U}|^2 dx dy = - \int_{R^2} \rho_t \delta E dx dy = - \int_{R^2} \rho \nabla (\delta E) \cdot \mathbf{U} dx dy. \quad (4.6)$$

To make this true for an arbitrary velocity field \mathbf{U} , it follows that $\mathbf{U} = -\nabla (\delta E)$. Substituting the velocity back to the continuity gives the evolution of the fluid density,

$$\epsilon \rho_t = \nabla \cdot (\rho \nabla (\delta E)), \quad (4.7)$$

$$\delta E = \frac{A}{\gamma} (-\epsilon^2 \Delta \rho + g'(\rho)) - \epsilon \omega, \quad (4.8)$$

subject to boundary conditions that requires no surface energy and no flux at the domain boundary,

$$\nabla \rho \cdot \hat{\mathbf{n}} = 0, \quad (4.9)$$

$$\rho \nabla (\delta E) \cdot \hat{\mathbf{n}} = 0. \quad (4.10)$$

Equations (4.7-4.8) with $\omega = 0$ constitute a fourth order Cahn-Hilliard equation with a degenerate mobility term. By letting ω having spatial dependence, we introduce electrowetting into the diffuse interface model.

5. Asymptotic analysis

Matched asymptotic expansions show the sharp interface limit of the constant-mobility Cahn-Hilliard equation approximates the two-side Mullins-Sekerka problem (see Caginalp & Fife 1988; Pego 1989). The recent work of Glasner (2003) showed the degenerate Cahn-Hilliard equation approaches the one-sided Hele-Shaw problem in the sharp interface limit. Using a similar method, we show that the sharp interface limit of the modified Cahn-Hilliard equation (4.7-4.8) recovers the Hele-Shaw problem with electrowetting (3.11-3.14). The diffuse interface approximation allows us to enact topology changes without artificial surgery of the contour. This is especially useful as electrowetting devices are designed for the purpose of splitting, merging and mixing of droplets.

Using a local orthogonal coordinate system (z, s) , where s denotes the distance along $\partial\Omega$ and z denotes signed distance to $\partial\Omega$, r , scaled by $1/\epsilon$. The dynamic equation expressed in the new coordinate is

$$\begin{aligned} \epsilon^2 \rho_z r_t + \epsilon^3 (\rho_s s_t + \rho_t) &= (\rho (\delta E)_z)_z + \epsilon \rho (\delta E)_z \Delta r + \epsilon^2 [\rho (\delta E)_s \Delta s + (\rho (\delta E)_s)_s |\nabla s|^2], \\ \delta E &= \frac{A}{\gamma} (-\rho_{zz} - \epsilon \rho_z \Delta r - \epsilon^2 (\rho_{ss} |\nabla s|^2 + \rho_s \Delta s) + g'(\rho)) - \epsilon \omega. \end{aligned}$$

The matching conditions are

$$\begin{aligned} \rho^{(0)}(z) &\sim \rho^{(0)}(\pm 0), \quad z \rightarrow \pm\infty, \\ \rho^{(1)}(z) &\sim \rho^{(1)}(\pm 0) + \rho_r^{(0)}(\pm 0) z, \quad z \rightarrow \pm\infty, \\ \rho^{(2)}(z) &\sim \rho^{(2)}(\pm 0) + \rho_r^{(1)}(\pm 0) z + \rho_{rr}^{(0)}(\pm 0) z^2, \quad z \rightarrow \pm\infty. \end{aligned}$$

Similar conditions can be derived for δE .

The $O(1)$ inner expansion gives

$$\left(\rho^{(0)} (\delta E^{(0)})_z \right)_z = 0, \quad (5.1)$$

$$\frac{A}{\gamma} \left(g'(\rho^{(0)}) - \rho_{zz}^{(0)} \right) = \delta E^{(0)}. \quad (5.2)$$

Equation (5.1) implies $(\delta E)^{(0)} = C(s, t)$. Equation (5.2) is the equation for the 1-D steady state. The common tangent construction implies

$$\delta E^{(0)} = \frac{\gamma(g(\rho_l) - g(\rho_v))}{A(\rho_l - \rho_v)}. \quad (5.3)$$

The double well structure of $g(\rho)$ implies $(\delta E)^{(0)} = 0$. At leading order the energy is expanded toward establishing a stable liquid-vapor interface.

The $O(1)$ outer expansion of (4.7), (4.8) gives

$$\nabla \cdot (\rho^{(0)} \nabla g'(\rho^{(0)})) = 0. \quad (5.4)$$

The unique solution in the dense phase that satisfies no flux and matching conditions is constant, $\rho^{(0)} = \rho_l$. Thus on an $O(1)$ scale no motion occurs.

The $O(\epsilon)$ inner expansion results

$$\left(\rho^{(0)} \left(\delta E^{(1)} \right)_z \right)_z = 0, \quad (5.5)$$

$$\frac{A}{\gamma} \left(g''(\rho^{(0)}) - \frac{\partial^2}{\partial z^2} \right) \rho^{(1)} = \delta E^{(1)} - \frac{A}{\gamma} \kappa^{(0)} \rho_z^{(0)} + \omega, \quad (5.6)$$

where the leading order curvature in the horizontal plane, $\kappa^{(0)}$, is identified with $-\Delta r$. Apply matching boundary condition for $\Delta E^{(1)}$ to equation (5.5) shows that $\Delta E^{(1)}$ is independent of z . $\rho^{(1)} = \rho_z^{(0)}$ is the homogenous solution of (5.6). In the region of constant ω , the solvability condition gives

$$\rho_l \left(\delta E^{(1)} \right) = A \kappa^{(0)} \int_{-\infty}^{\infty} \frac{(\rho_z^{(0)})^2}{\gamma} dz - \omega \rho_l. \quad (5.7)$$

The integral equals to 1 by applying (4.4). Assuming $\rho_l = 1$ and using (3.15) give

$$\delta E^{(1)} = \left(A \kappa^{(0)} + B \kappa_1 \right). \quad (5.8)$$

The surface energy term includes both curvatures of the interface. This is analogous to the Laplace-Young condition of a liquid-vapor interface.

In regions where sharp variation of ω intersects the diffuse interface, the solvability

condition becomes

$$\rho_l \left(\delta E^{(1)} \right) = A\kappa^{(0)} - \int_{-\infty}^{\infty} \omega \rho_z^{(0)} dz. \quad (5.9)$$

The sharp surface energy variation is smoothly weighted by $\rho_z^{(0)}$, which is $O(1)$ for a phase function ρ that varies smoothly between 0 and 1 in the scaled coordinate.

To order ϵ , the outer equation in the dense phase must solve

$$\Delta \left(\delta E^{(1)} \right) = 0, \quad (5.10)$$

with a no flux boundary condition in the far field, and a matching condition at the interface described by (5.1).

The $O(\epsilon^2)$ inner expansion reveals the front movement

$$U^{(0)} \rho_z^{(0)} = \left(\rho^{(0)} \left(\delta E^{(2)} \right)_z \right)_z, \quad (5.11)$$

where r_t is identified as the leading order velocity $U^{(0)}$. Matching condition for $\delta E^{(2)}$ gives us the relation for the normal interface velocity of droplets in Hele-Shaw cell,

$$U^{(0)} = - \left(\delta E^{(1)} \right)_r. \quad (5.12)$$

Defining $\tilde{p} = \delta E^{(1)}$, equations (5.8) (5.10) and (5.12) constitute the sharp interface Hele-Shaw flow with electrowetting,

$$\Delta \tilde{p} = 0,$$

$$\tilde{p}|_{\partial\Omega} = A\kappa^{(0)} + B\kappa_1,$$

$$U^{(0)} = - (\tilde{p})_r.$$

6. Numerical simulations and discussion

Numerical methods for solving the nonlinear Cahn-Hilliard equation is an active area of research. Barrett, Blowey & Garcke (1999) proposed a finite element scheme to solve the fourth order equation with degenerate mobility. In addition, the development of numerical

methods for solving thin film equations (see Zhornitskaya & Bertozzi 2000; Grun & Rumpf 2000; Witelski & Bowen 2003) are also applicable to (4.7-4.8). We discretize the equations by finite differencing in space with a semi-implicit timestep,

$$\epsilon \frac{\rho_{n+1} - \rho_n}{\Delta t} + \frac{A\epsilon^2 M}{\gamma} \Delta^2 \rho_{n+1} = \frac{A}{\gamma} [\epsilon^2 \nabla \cdot ((M - \rho_n) \nabla \Delta \rho_n) + \nabla \cdot (\rho_n \nabla g'(\rho_n))] - \nabla \cdot (\rho_n \epsilon \omega). \quad (6.1)$$

We use a simple polynomial $g(\rho) = (\rho - \rho_v)^2(\rho - \rho_l)^2$. The choice of $g(\rho)$ imposes an artificial value of the liquid-vapor surface energy, γ . Integrating (4.4) gives the normalizing parameter, $\gamma = 0.2322$, for the terms associated with the liquid-vapor interface. All numerical results here are computed on a 256 by 128 mesh with $\Delta x = 1/30$ and $\epsilon = 0.0427$.

A convexity splitting scheme is used where the scalar M is chosen large enough to improve the numerical stability. We found $M = \max(\rho)$ serves this purpose. The equation can be solved efficiently through fast Fourier transform methods. Similar ideas were also used to simulate coarsening in the Cahn-Hilliard equation (Vollmayr-Lee & Rutenberg 2003) and surface diffusion (Smereka 2003). The diffuse interface model imposes a constraint on the spatial resolution in order to resolve the transition layer, $\Delta x \leq C\epsilon$. Preconditioning techniques maybe implemented to relax this constraint (see Glasner 2001). We did not employ preconditioning in this study.

To test our scheme, we compare the diffuse interface scheme against the boundary integral method by simulating the relaxation of an elliptical droplet in a Hele-Shaw cell without electrowetting. Figure 7 shows a close agreement between the aspect ratios of the relaxing elliptic droplets calculated by both methods.

To investigate the dynamics of electrowetting droplet without contact line dissipation, equation (6.1) corresponds to the sharp interface model with $A\kappa_0 = 1$ and $B\kappa_1 = -\omega$. We directly compare the diffuse interface model to the electrowetting experiments with a 60%

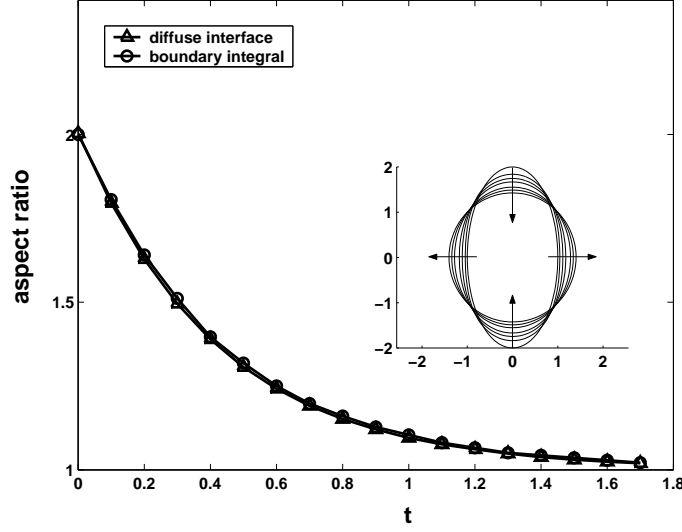


FIGURE 7. Aspect ratio of the relaxing elliptic droplet calculated by diffuse interface model (\triangle) with $\epsilon = 0.0427$ and boundary integral method, (\circ).

glycerine-water mixture. The experimental time and dimensions are scaled according to equation (3.10). The dimension of the square electrode is 1 cm. The radii of the droplets in figure 8 and 9 are approximately 0.6 mm and 0.55 mm respectively. Using (3.15), the electrowetting numbers are $\omega = 7.936$ and 7.273 respectively, corresponding to the application of 50.42 V DC voltage. Figure 8b illustrates the capability of the method to naturally simulate the macroscopic dynamics of a droplet splitting. The resolution of the model is limited by the diffuse interface thickness. Therefore we do not expect the simulation to reproduce the formation of satellite droplets as seen in the last few frame of figure 8b. The comparison between the simulation result and the actual images of a droplet in translation shows an overestimation of the electrowetting effect (figure 9b). The experiment is slower than the numerical result by a factor of 2. The disagreement of timescales is more severe for droplet splitting. We will discuss the role of contact line

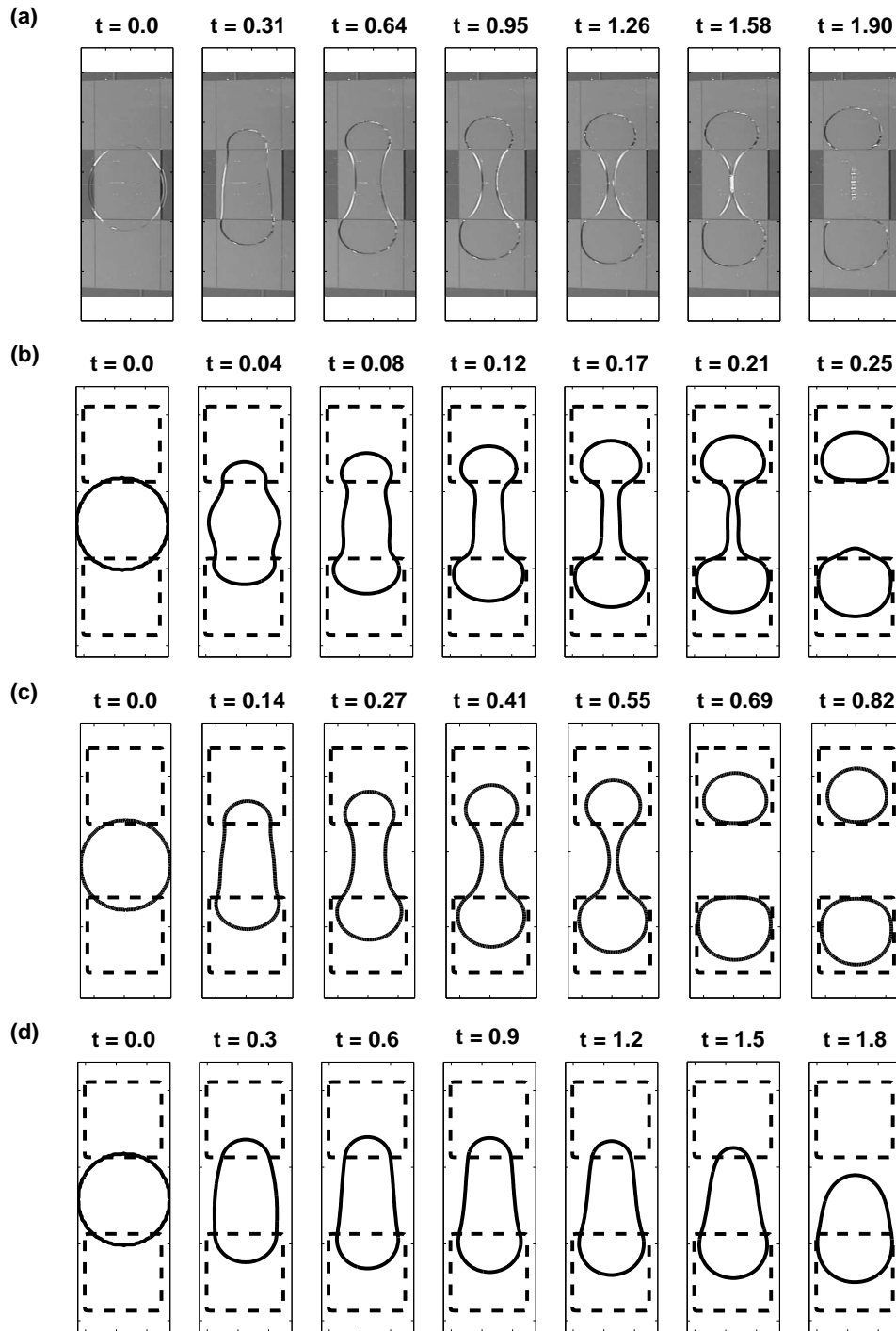


FIGURE 8. Droplet splitting by electrowetting (a) images of a droplet pulled apart by two electrodes under 50.42 volts of potential, (b) diffuse interface model with $\omega = 7.936$, (c) $\omega = 3.968$, and (d) $\omega = 1.818$.

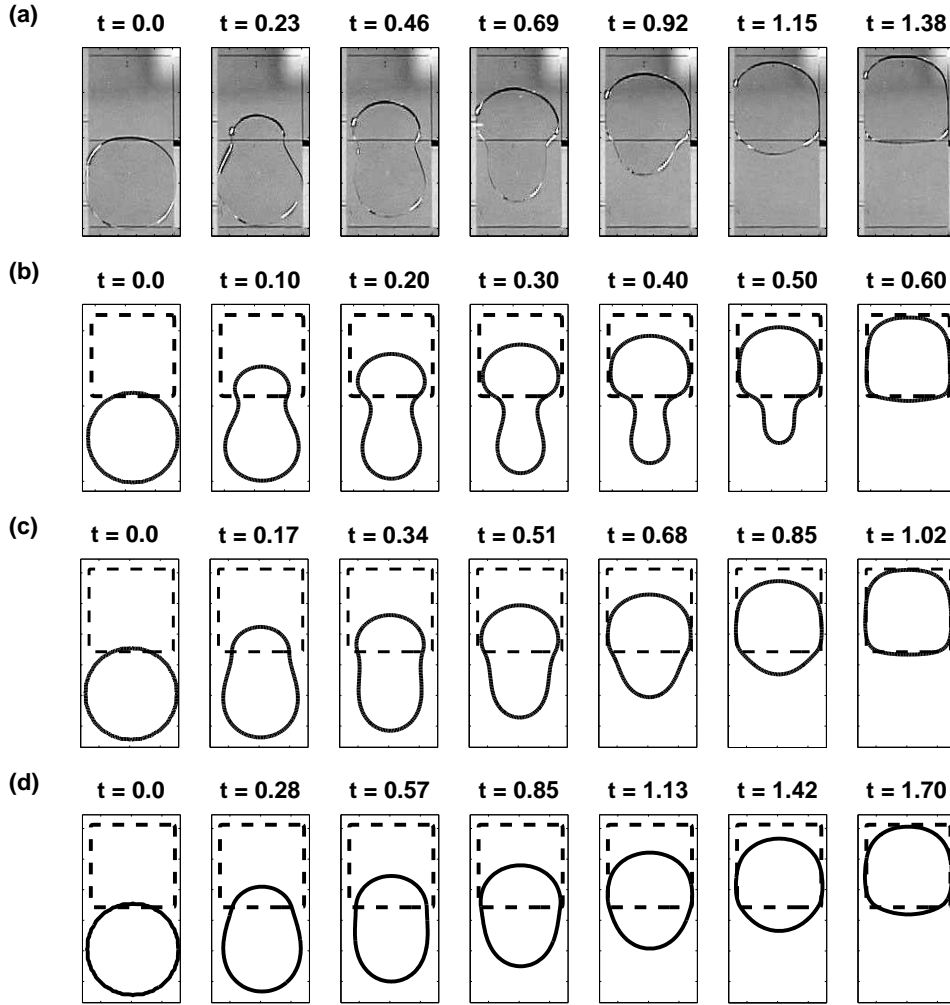


FIGURE 9. Droplet movement by electrowetting: (a) images of a droplet translate to an electrode under 50.42 volts of potential, (b) diffuse interface model with $\omega = 7.273$, (c) $\omega = 3.636$, and (d) $\omega = 1.818$.

in the next section; we argue that the contact line dynamics is more than adequate to account for this discrepancy.

Comparing the droplet motion between figure 9b-d shows the gradually dominating trend of the relaxation timescale due to bulk surface tension as the electrowetting number is decreased. The droplet morphologies transition from the ones with drastic variation in the horizontal curvature to rounded shapes with small variation in the horizontal curva-

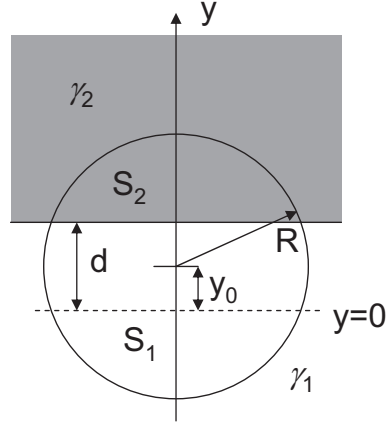


FIGURE 10. Approximation of droplet travels as solid circle under influence of electrowetting by a semi-infinite electrode.

ture. 8d serves as a illustration of the competition between the two dynamic timescales. Electrowetting initially creates the variation of $B\kappa_1$ to stretch the droplet. As the droplet stretches, the convection slows due to the decreasing pressure in the necking region and increasing pressure in the two ends. Ultimately, the relaxation process takes over to pump the fluid in the end with larger curvature toward the end with smaller curvature.

7. Contact line effect

The previous sections investigate the droplet dynamics in the absence of additional contact line effects due to the microscopic physics of the surface (see deGennes 1985). The dynamics near the contact line results in a stress singularity at the contact line (see Huh & Scriven 1971; Dussan 1979) and is still an active area of research. These factors have contributed to the lack of an unified theory for the contact line dynamics. Inclusion of van der Waal potential in the diffuse interface model has recently been proposed as a regularization of a slowly moving contact line of a partially wetting fluid (see Pomeau 2002; Pismen & Pomeau 2004). Here, we estimate the range of slowdown that is caused contact line dissipation.

In order to estimate the contact line influence on the diffuse interface model, we construct a reduced order approximation of the diffuse interface model by considering the droplet as a solid circle moving toward a semi-infinite electrowetting region as shown in figure 10. The approximation examines the dynamics in the limit of small horizontal curvature variation to isolate the contact line effect on the dynamic timescale. The position of the center of the circle can be derived by considering the rate of free energy decrease as outlined in appendix A.

$$z = \sin \left(\frac{b\Delta\gamma}{6\mu\pi R^2} t + C \right), \quad C = \arcsin \frac{d}{R}, \quad (7.1)$$

where d is the distance between the boundary of the electrowetting region to the origin, and $z = (d - y_0)/R$ is the signed distance from the center of the circle to the boundary of the electrowetting region normalized by the radius.

If there is no contact line dissipation, the energy difference between the two regions is well described by (1.1), $\Delta\gamma = -CV^2/2$. After changing time to a dimensionless variable, we get

$$z = \sin \left(\frac{-2\omega}{\pi} t + C \right). \quad (7.2)$$

As a droplet translates from one electrode from another, z varies from d/R to -1 . The dynamic timescale is thus inversely proportional to the electrowetting voltage applied. Figure 11 compares the diffuse interface model with the prediction by the reduced order model. Electrowetting quickly pumps the droplet into the wetting region. During the motion, the droplet readily deforms its free surface. Once the entire droplet has moved into the wetting region, slow relaxation toward a circular shape takes place. The close agreement with the diffuse interface model shows our model does accurately simulate the gradient flow of the energy functional. The experimental timescale discrepancies shown in figures 8 and 9 must be attributed to additional dissipation in the physical problem.

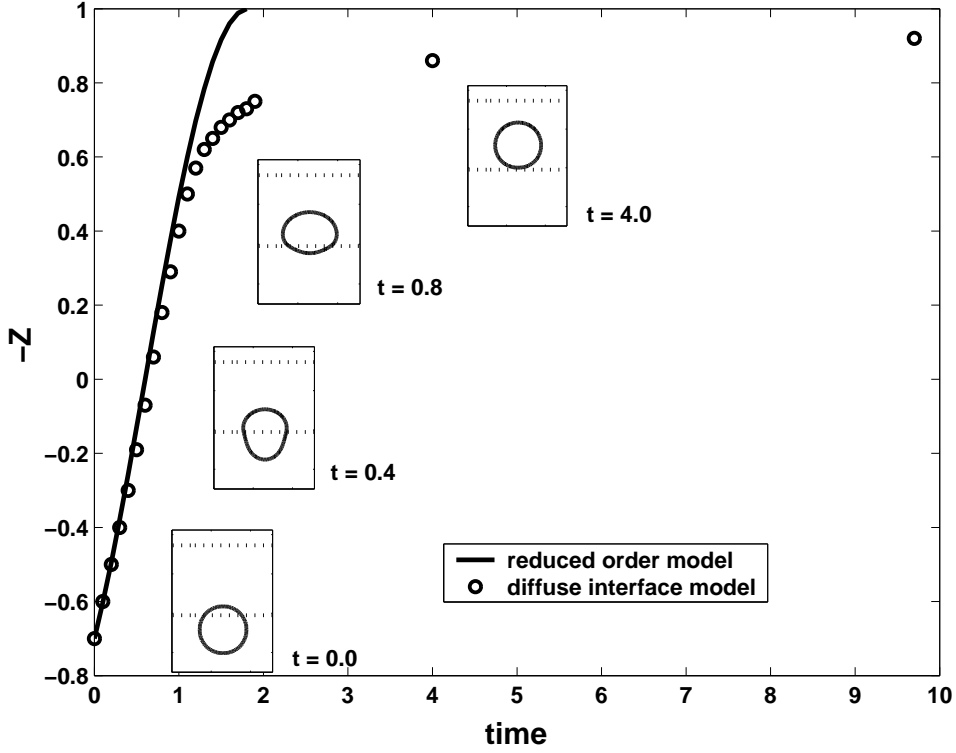


FIGURE 11. Comparison reduced order model and diffuse interface model of a droplet translation into a semi-infinite electrowetting . $\epsilon = 0.0427$. $\omega = 5.0512$

Surface heterogeneities introduces an additional dissipation that must be overcome by the moving contact line. This dissipation causes the dynamic contact angles to increase along the advancing contact lines to increase and decrease along the receding contact. In the context of our reduced order model, the effective surface energy decrease that drives the droplet becomes

$$\Delta\gamma = \gamma_{lv} (\cos\theta_r - \cos\theta_t + \cos\theta_r - \cos\theta_b). \quad (7.3)$$

where θ_r is the dynamic contact angle on the receding contact lines. θ_t and θ_b are the dynamic contact angles on the advancing contact line on the top substrate and the bottom substrate respectively. Similar concepts of contact line dissipation have been proposed by Ford & Nadim (1994) and Chen, Troian, Darhuber & Wagner (2005) in the

context of a thermally driven droplet. Comparing the new energy description against the electrowetting potential gives

$$\xi = \frac{\Delta\gamma}{-CV^2/2} = \frac{(\cos\theta_r - \cos\theta_t) + (\cos\theta_r - \cos\theta_b)}{\cos\theta_0 - \cos\theta_v}. \quad (7.4)$$

where $\cos\theta_b < \cos\theta_v$, $\cos\theta_t < \cos\theta_0$, and $\cos\theta_r > \cos\theta_0$. It can be shown that the scalar ξ is less than 1. The addition of contact line dissipation may be incorporated into the reduced order model by a scaling the electrowetting number accordingly,

$$z = \sin\left(\frac{-2\xi\omega}{\pi}t + C\right). \quad (7.5)$$

Substituting in the measured values of dynamic contact angles from figure 4 gives an estimate of $\xi = 0.2313$. This indicates the contact line may dissipate up to 3/4 of the electrowetting potential and account for a four fold increase in the dynamic timescale.

To understand the contact line influence on a sharp interface droplet with small aspect ratio, α , we relate the pressure boundary condition (3.3) to the local contact angle by perturbation expansions of the governing equations with respect to the aspect ratio and enforcing the solutions of the liquid meniscus to form a prescribed contact angle with the solid substrates in the lowest order. The leading order expansion then relates the cross substrate curvature, $B\kappa_1$, to the local dynamic contact angle, and the next order expansion corresponds to the contribution from the horizontal curvature, $A\kappa_0$.

Outside of the electrowetting region, the interface is symmetric and the pressure boundary condition is

$$P|_{\partial\Omega} = \frac{-2\cos\theta_s}{\alpha} - \frac{1 + \sin\theta_s}{\cos\theta_s} \left(\frac{\theta_s}{2} - \frac{\pi}{4}\right) + O(\alpha^2), \quad (7.6)$$

where θ_s denotes the contact angle of the symmetric interface. If the interface inside the electrowetting region satisfy the requirements that $\theta_t \geq \pi/2$ and $\theta_b \leq \pi/2$, we can

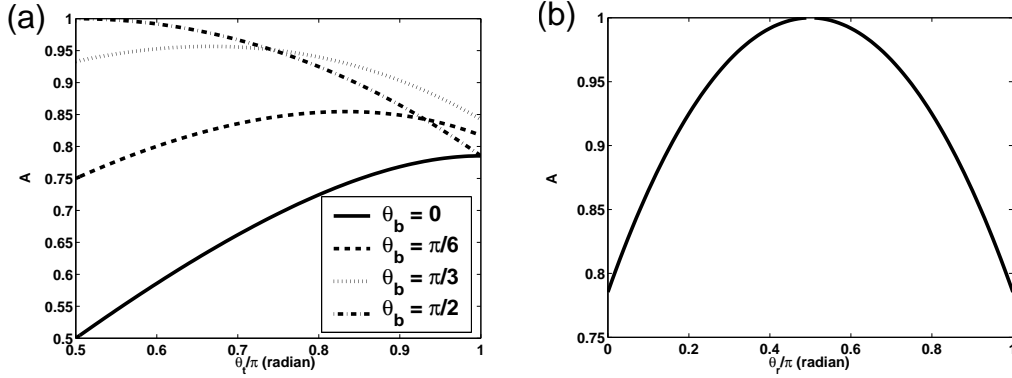


FIGURE 12. Horizontal curvature A for (a) electrowetting and (b) non-electrowetting menisci.

perform similar expansions for an interface inside of the electrowetting region,

$$P|_{\partial\Omega} = \frac{-(\cos\theta_b + \cos\theta_t)}{\alpha} - \frac{\cos\theta_t}{2(1 - \cos(\theta_b - \theta_t))} \left(\frac{\cos\theta_b}{\cos\theta_t} \sin(\theta_b - \theta_t) + \theta_t - \theta_b \right) + O(\alpha^2). \quad (7.7)$$

For the interface outside of the electrowetting region, inspection of the $O(\alpha)$ term of (7.6) shows A varies between a maximum of 1 when $\theta_r = \pi/2$ and a minimum of $\pi/4$ when $\theta_r = 0$ and π , as derived by Park & Homsy (1984). For the interface inside of the electrowetting region, A varies between a maximum value of 1.0 when $\theta_b = \theta_t = \pi/2$ and a minimum of 0.5 at $\theta_b = 0$ and $\theta_t = \pi/2$. Since relaxation dominates away from the boundary of the electrowetting region, we can obtain good estimate of A by substituting the data in figure 4. The computed values of A are 0.9994 and 0.9831 for the interfaces outside and inside of the electrowetting region respectively.

Analysis of sharp interface model in §3 shows the velocity of the electrowetting droplet is directly related to the difference of $B\kappa_1$ across the boundary of the electrowetting region. Taking the difference of the leading order terms in (7.6) and (7.7) gives the curvature difference in the presence of contact line dissipation,

$$[B\kappa_1] = \frac{1}{\alpha} (\cos\theta_s - \cos\theta_t + \cos\theta_s - \cos\theta_b), \quad (7.8)$$

where the interface curvatures, and the associated dynamic contact angles must be close to the boundary of the electrowetting region.

Using (3.15) and (3.8) we can obtain $[B\kappa_1]$ without the contact line dissipation, which is just the difference of electrowetting number,

$$[B\kappa_1] = -\frac{CV^2}{2\alpha\gamma_{lv}} = \frac{1}{\alpha} (\cos\theta_0 - \cos\theta_v). \quad (7.9)$$

The ratio of the curvature difference leads to the same formula as (7.4). However, the dynamic contact angles in (7.8) is associated with the interface near the boundary of the electrowetting region. In contrast, the estimate by the reduced order model utilizes the geometries at the nose and the tail of the droplet where the contact line dynamics has more significant effect on the interface. Therefore we expect the estimate by the reduced order model to provide only an upper bound to the contact line effect. With 1/4 reduction of the electrowetting number as estimated by the reduced order model, figures 8d and 9d show slower droplet motions than the experiments. Figure 8d shows the failure to split the droplet, confirming that the estimate indeed overestimates the contact line dissipation. Lacking the contact angle measurements near the electrowetting boundary, we compute the droplet motion with less severe reduction (1/2) of the electrowetting number shown in figures 8c and 9c. The close agreement of the droplet motion indicates that refinements to our worse case estimate with the correct geometries may substantially improve the model.

In addition to its influence on the convective timescale, the contact line dissipation also effects the morphology of the droplet motion. Therefore, a complete model of the contact line dynamics needs to address both the effect on $A\kappa_0$ and $B\kappa_1$. This differs from the scaling factor in Walker & Shapiro (2004) that phenomenologically modifies the dynamic timescale to fit with the experiments.

8. Conclusions

We present a diffuse interface description of the droplets in a Hele-Shaw cell in the form of a degenerate Cahn-Hilliard equation with a spatially varying surface energy. Through matching asymptotic expansions, we show that the phase field approach approximates the sharp interface Hele-Shaw flow in the limit of small diffuse interface thickness. The dynamics in sharp interface limit is validated numerically by a direct comparison to the boundary integral methods. This approach enables us to naturally simulate the macroscopic dynamics of droplet splitting, merging, and translation under the influence of local electrowetting.

For a viscous droplet of larger aspect ratio, the velocity component normal to the substrates becomes significant to the dynamics. In this case, the 2-D Hele-Shaw model can no longer provide adequate approximation. On the other hand, a fully three-dimensional simulation of such a droplet is an extremely complicated task. It would be desirable to develop a reduced dimension model that is computationally tractable model while preserving the essential information about the velocity component normal to the substrates. Such a model will be valuable to the study of fluid mixing inside of an electrowetting droplet.

As illustrated by the perturbation analysis and the reduced order model, the contact line dynamics complicates the problem by modifying both the cross substrate and horizontal curvatures of the interface. The viscosity terms effects the perturbation analysis at $O(Ca)$. However, viscous stress singularity at the contact line indicates more physics is required to regularize the fluid dynamic formulation near the contact line. Base on the measured advancing and receding contact angles, we showed the strong influence of contact line dynamics accounts up to a four fold increase in the dynamic timescale of the Hele-Shaw approximation. Knowledge of the geometries near the electrowetting region

boundary may provide improvement to our estimate. Numerical simulations of droplet motions showed a range of dynamic timescale that is consistent with the experimentally measured timescale.

We thank Pirouz Kavehpour for invaluable experimental support, and discussions on contact line dynamics. We gratefully acknowledge valuable discussions of Hele-Shaw cell with George M. Homsy, and Sam D. Howison. We also thank Hamarz Aryafar and Kevin Lu for their expertise and assistance in the use of high speed camera and rheometer. This work was supported by ONR grant N000140410078, NSF grant DMS-0244498, NSF grant DMS-0405596, and NASA through Institute for Cell Mimetic for Space Exploration (CMISE).

Appendix A. Reduced order model

Consider a semi-infinite electrowetting region, we approximate the droplet motion as a moving solid circle. Using the lubrication approximation, we balance the rate of viscous dissipation with the rate of free energy decrease,

$$D \approx -\frac{b^3}{12\mu} \int_{R^2} \rho |\nabla p|^2 dx dy = -\frac{12\mu}{b} \int_{R^2} \rho |\mathbf{U}|^2 dx dy = \frac{dE}{dt} \quad (\text{A } 1)$$

The center of the circle travels along the axis as shown in figure 10. The distance between the boundary of electrowetting region and the origin is d . The position of the center is $y_0(t)$ where $y_0(0) = 0$. The droplet moves as a solid circle so the integral reduces to

$$-\frac{12\mu |\dot{y}_0|^2 \pi R^2}{b} = \frac{dE}{dt}, \quad (\text{A } 2)$$

where \dot{y}_0 denotes the velocity of the center of the circle. The free energy is composed of the surface energy of dielectric surface with no voltage applied γ_1 , the surface energy of the electrowetting region γ_2 , and the liquid-vapor surface energy. Since the liquid-vapor

interface area remains constant, the rate of change in free energy is

$$\frac{dE}{dt} = \Delta\gamma\dot{S}_2, \quad (\text{A } 3)$$

where $\Delta\gamma = \gamma_2 - \gamma_1$ and \dot{S}_2 is the derivative of the droplet area inside the electrified region with respect to time

$$\dot{S}_2 = -2R^2\sqrt{1-z^2}\dot{z}, \quad (\text{A } 4)$$

where $z = (d - y_0)/R$ is the signed distance from the center of the circle to the boundary of electrowetting region normalized by the droplet radius. (A 2), (A 3), and (A 4) give the following ODE:

$$\dot{z} = \frac{b\Delta\gamma}{6\mu\pi R^2}\sqrt{1-z^2}. \quad (\text{A } 5)$$

Integrate this ODE we get

$$z = \sin\left(\frac{b\Delta\gamma}{6\mu\pi R^2}t + C\right), \quad C = \arcsin\frac{d}{R}, \quad (\text{A } 6)$$

REFERENCES

- BARRETT, J. W., BLOWEY, J. F. & GARCKE, H. 1999 Finite element approximation of the Cahn-Hilliard equation with degenerate mobility. *SIAM J. Numer. Anal.* **37**, 286–318.
- BENSIMON, D., KADANOFF, L. P., LIANG, S. & SHRAIMAN, S. 1986 Viscous flow in two dimensions. *Rev. Mod. Phys.* **58**, 977–999.
- BRETHERTON, F. P. 1961 The motion of long bubble in tubes. *J. Fluid Mech.* **10**, 166–188.
- CAGINALP, G. & FIFE, P. 1988 Dynamics of layered interfaces arising from phase boundaries. *SIAM J. Appl. Math.* **48**, 506–518.
- CHEN, J. Z., TROIAN, S. M., DARHUBER, A. A. & WAGNER, S. 2005 Effect of contact angle hysteresis on thermocapillary droplet actuation. *J. Appl. Phys.* **97**, 014906.
- CHO, S.-K., MOON, H. & KIM, C.-J. 2003 Creating, transporting, cutting, and merging liquid droplets by electrowetting-based actuation for digital microfluidic circuits. *J. Microelectromech. Syst.* **12**, 70–80.

- CHOUKE, R. L., VAN MEURS, P. & VAN DER POEL, C. 1959 The instability of slow, immiscible viscous liquid-liquid displacements in permeable media. *Trans. AIME* **216**, 188–194.
- DARHUBER, A. & TROIAN, S. M. 2005 Principles of microfluidic actuation by manipulation of surface stresses. *Annu. Rev. Fluid Mech.* **37**, 425–455.
- DEGENNES, P. G. 1985 Wetting: statics and dynamics. *Rev. Mod. Phys.* **57**, 827–863.
- DUSSAN, E. B. 1979 On the spreading of liquid on solid surfaces: static and dynamic contact lines. *Ann. Rev. Fluid Mech.* **11**, 371–400.
- FORD, M. L. & NADIM, A. 1994 Thermocapillary migration of an attached drop on a solid surface. *Phys. Fluids* **6**, 3183–3185.
- GLASNER, K. 2001 Nonlinear preconditioning for diffuse interfaces. *J. Comp. Phys.* **174**, 695–711.
- GLASNER, K. 2003 A diffuse interface approach to Hele-Shaw flow. *Nonlinearity* **16**, 49–66.
- GRUN, G. & RUMPF, M. 2000 Nonnegativity preserving convergent schemes for the thin film equation. *Numer. Math.* **87**, 113–152.
- HAYES, R. A. & FEENSTRA, B. J. 2003 Video-speed electronic paper based on electrowetting. *Nature* **425**, 383–385.
- HELE-SHAW, H. S. 1898 The flow of water. *Nature* **58**, 34–36.
- HOMSY, G. M. 1987 Viscous fingering in porous media. *Ann. Rev. Fluid Mech.* **19**, 271–311.
- HOU, T., LOWENGRUB, J. S. & SHELLY, M. J. 1994 Removing the stiffness from interfacial flow with surface-tension. *J. Comp. Phys.* **114**, 312–338.
- HOWISON, S. D. 1992 Complex variable methods in Hele-Shaw moving boundary problems. *Eur. J. Appl. Maths* **3**, 209–224.
- HUH, C. & SCRIVEN, L. E. 1971 Hydrodynamic model of steady movement of a solid-liquid-fluid contact line. *J. Coll. Int. Sci.* **35**, 85–101.
- KANG, K. H. 2002 How electrostatic fields change contact angle in electrowetting. *Langmuir* **18**, 10318–10322.
- KOHN, R. V. & OTTO, F. 1997 Small surface energy, coarse-graining, and selection of microstructure. *Physica D* **107**, 272–289.

- KOPFSILL, A. R. & HOMSY, G. M. 1988 Bubble motion in a Hele-Shaw cell. *Phys. Fluids* **31**, 18–26.
- LEE, H., LOWENGRUB, J. S. & GOODMAN, J. 2002*a* Modeling pinchoff and reconnection in a Hele-Shaw cell. i. the models and their calibration. *Phys. Fluids* **14**, 492–513.
- LEE, J., MOON, H., FOWLER, J., SCHOELLHAMMER, J. & KIM, C.-J. 2002*b* Electrowetting and electrowetting-on-dielectric for microscale liquid handling. *Sensors and Actuators A* **95**, 259–268.
- LIPPMAN, M. G. 1875 Relations entre les phénomènes électriques et capillaires. *Ann. Chim. Phys.* **5**, 494–548.
- MAXWORTHY, T. 1986 Bubble formation, motion and interaction in a Hele-Shaw cell. *J. Fluid Mech.* **173**, 95–114.
- MOON, H., CHO, S.-K., GARREL, R. L. & KIM, C.-J. 2004 Electrowetting-based microfluidics for analysis of peptides and proteins by matrix-assisted laser desorption/ionization mass spectrometry. *Anal. Chem.* **76**, 4833–4838.
- OTTO, F. 1998 Dynamics of labyrinthine pattern formation in magnetic fluids: A mean-field theory. *Arch. Rat. Mech. Anal.* **141**, 63–103.
- PARK, C.-W. & HOMSY, G. M. 1984 Two-phase displacement in Hele-Shaw cells: theory. *J. Fluid Mech.* **139**, 291–308.
- PARK, C. W., MARUVADA, S. R. K. & YOON, D. Y. T. 1994 The influence of surfactants on the bubble motion in Hele-Shaw cells. *Phys. Fluids* **6**, 3267–3275.
- PEGO, R. L. 1989 Front migration in the nonlinear cahn hilliard equation. *Proc. R. Soc. Lond. A* **422**, 261–278.
- PEYKOV, V., QUINN, A. & RALSTON, J. 2000 Electrowetting: a model for contact-angle saturation. *Colloid. Polym. Sci.* **278**, 789–793.
- PISMEN, L. M. & POMEAU, Y. 2004 Mobility and interactions of weakly nonwetting droplets. *Phys. Fluids* **16**, 2604–2612.
- POLLACK, M. G., FAIR, R. B. & SHENDEROV, A. D. 2000 Electrowetting-based actuation of liquid droplets for microfluidic applications. *Appl. Phys. Lett* **77**, 1725–1726.

- POLLACK, M. G., SHENDEROV, A. D. & FAIR, R. B. 2002 Electrowetting-based actuation of droplets for integrated microfluidics. *Lab on a Chip* **2**, 96–101.
- POMEAU, Y. 2002 Recent progress in the moving contact line problem: a review. *C. R. Mécanique* **330**, 207–222.
- REINELT, D. A. 1987 Interface conditions for two-phase displacement in Hele-Shaw cells. *J. Fluid Mech.* **184**, 219–234.
- SAFFMAN, P. G. 1986 Viscous fingering in Hele-Shaw cells. *J. Fluid Mech.* **173**, 73–94.
- SEYRAT, E. & HAYES, R. A. 2001 Amorphous fluoropolymers as insulators for reversible low-voltage electrowetting. *J. Appl. Phys.* **90**, 1383–1386.
- SMERKA, P. 2003 Semi-implicit level-set method for curvature and surface diffusion motion. *J. Sci. Comp.* **19**, 439–456.
- TANVEER, S. 1986 The effect of surface-tension on the shape of a Hele-Shaw cell bubble. *Phys. Fluids* **29**, 3537–3548.
- TANVEER, S. 1987 New solutions for steady bubbles in a Hele-Shaw cell. *Phys. Fluids* **30**, 651–668.
- TANVEER, S. 2000 Surprises in viscous fingering. *F. Fluid Mech.* **409**, 273–308.
- TANVEER, S. & SAFFMAN, P. G. 1987 Stability of bubbles in Hele-Shaw cell. *Phys. Fluids* **30**, 2624–2635.
- TANVEER, S. & SAFFMAN, P. G. 1989 Prediction of bubble velocity in a Hele-Shaw cell - thin-film and contact-angle effects. *Phys. Fluids A* **1**, 219–223.
- TAYLOR, G. & SAFFMAN, P. G. 1958 The penetration of a fluid into a porous medium or Hele-Shaw cell containing a more viscous liquid. *Proc. R. Soc. Lond. A* **245**, 312–329.
- TAYLOR, G. & SAFFMAN, P. G. 1959 A note on the motion of bubbles in a Hele-Shaw cell and porous medium. *Q. J. Mech. Appl. Math.* **12**, 265–279.
- VALLET, M., VALLADE, M. & BERGE, B. 1999 Limiting phenomena for the spreading of water on polymer films by electrowetting. *Eur. Phys. J.* **B11**, 583–591.
- VERHEIJEN, H. J. J. & PRINS, M. W. J. 1999 Reversible electrowetting and trapping of charge: model and experiments. *Langmuir* **15**, 6616–6620.

- VOLLMAYR-LEE, B. P. & RUTENBERG, A. D. 2003 Fast and accurate coarsening simulation with an unconditionally stable time step. *Phys. Rev. E* **68**, 066703.
- WALKER, S. & SHAPIRO, B. 2004 Modeling the fluid dynamics of electro-wetting on dielectric (ewod). *JMEMS*. (submitted).
- WHEELER, A. A., MOON, H., KIM, C.-J., LOO, J. A. & GARREL, R. L. 2004 Electrowetting-based microfluidics for analysis of peptides and proteins by matrix-assisted laser desorption/ionization mass spectrometry. *Anal. Chem.* **76**, 4833–4838.
- WITELSKI, T. P. & BOWEN, M. 2003 Adi schemes for higher-order nonlinear diffusion equations. *Appl. Numer. Math.* **45**, 331–351.
- ZHORNITSKAYA, L. & BERTOZZI, A. L. 2000 Positivity-preserving numerical schemes for lubrication-type equations. *SIAM J. Numer. Anal.* **37**, 523–555.